Flavoring the production of Higgs boson pairs

M. A. Arroyo-Ureña,[1,2,*] J. Lorenzo Díaz-Cruz,[1,2,†] E. A. Herrera-Chacón,[3,‡] T. A. Valencia-Pérez,[4,§] and J. Mejia Guisao[5,2,∥]

[1]*Facultad de Ciencias Físico-Matemáticas, Benemérita Universidad Autónoma de Puebla, C.P. 72570, Puebla, México*
[2]*Centro Interdisciplinario de Investigación y Enseñanza de la Ciencia (CIIEC), Benemérita Universidad Autónoma de Puebla, C.P. 72570, Puebla, México*
[3]*Institute for Particle Physics Phenomenology, Durham University, South Road, Durham, DH1 3LE, United Kingdom*
[4]*Instituto de Física, Universidad Nacional Autónoma de México, C.P. 01000, Ciudad de México, México*
[5]*Departamento de Física, Centro de Investigación y de Estudios Avanzados del Instituto Politécnico Nacional, Ciudad de México, AP 14740, CP 07000, México*

(Received 1 November 2024; accepted 6 March 2025; published 26 March 2025)

We present a study on the possibility of observing a hypothetical particle known as the flavon H_F, which is predicted in an extension of the standard model that includes the so-called Froggatt-Nielsen mechanism. The proposed decay channel is through a $b\bar{b}h$ final state, where the Higgs boson (h) decays to a pair of photons or a pair of b quarks $(h \to \gamma\gamma, b\bar{b})$. We found that, under special scenarios of the model parameter space, the processes analyzed could provide evidence for the existence of the flavon in the next stage of the LHC: the High Luminosity LHC. Specifically, we predict a *signal significance* of 5σ (2σ) in the $h \to b\bar{b}$ $(h \to \gamma\gamma)$ channel for a flavon mass of 800 (900) GeV and an integrated luminosity of 2500 (3000) fb^{-1}.

DOI: 10.1103/PhysRevD.111.055028

I. INTRODUCTION

After the discovery of the Higgs boson by the ATLAS and CMS Collaborations [1,2] at the Large Hadron Collider (LHC), the particle physics community has focused on understanding the interactions of the Higgs boson with other particles, including itself. In the last years, the ATLAS and CMS Collaborations have reported results on searches for di-Higgs proton-proton (pp) production in the channels $pp \to hh$, $(h \to b\bar{b}, h \to b\bar{b})$, $(h \to b\bar{b}, h \to \gamma\gamma)$, $(h \to b\bar{b}, h \to WW^*)$, $(h \to b\bar{b}, h \to ZZ^*)$, $(h \to b\bar{b}, h \to \tau^-\tau^+)$ [3–7]. These searches have studied the different ways in which the Higgs boson is produced, such as ggh, vector boson fusion, in association with top-quark pairs, etc. We notice that in all channels the $b\bar{b}$ pair prevails; motivated by these final states we undertake an analysis of production and decay of a scalar (so-called flavon, denoted by H_F) predicted in a model that implements the Froggatt-Nielsen (FN) mechanism [8], which we will refer to as the FN singlet model (FNSM). Such a model assumes that above some scale Λ, there is a symmetry [perhaps of Abelian type $U(1)_F$] that forbids the appearance of Yukawa couplings; SM fermions are charged under this symmetry. However, Yukawa matrices can arise through nonrenormalizable operators. The Higgs spectrum of these models includes the flavon, which could mix with the Higgs bosons when the flavor scale is of the order of the TeVs. The flavon phenomenology has been studied by several authors, including the production and decay processes $pp \to H_F \to hh(h \to \gamma\gamma, h \to b\bar{b})$, $pp \to H_F \to ZZ(Z \to \ell^-\ell^+)$, $pp \to H_F \to tc(t \to \ell\nu_\ell b)$, $pp \to H_F \to \tau\mu(\tau \to \ell\nu_\tau\nu_\ell)$ $(\ell = e, \mu)$ [9–13]. In this study, we explore a final state in which current experimental reports on searches for the di-Higgs boson can shed light on the signal we propose, i.e., the production of the flavon via proton-proton collisions, and later it decays into $b\bar{b}h$ for two particular channels, namely $h \to b\bar{b}$ and $h \to \gamma\gamma$. The induced Feynman diagrams of the decay $H_F \to f\bar{f}h$ in the theoretical framework of the FNSM are presented in Fig. 1.[1] The main difference between the di-Higgs boson

*Contact author: marco.arroyo@fcfm.buap.mx
†Contact author: jldiaz@fcfm.buap.mx
‡Contact author: edwin.a.herrera-chacon@durham.ac.uk
§Contact author: tvalencia@fisica.unam.mx
∥Contact author: jhovanny.andres.mejia.guisao@cern.ch

[1]The diagram (b) has a scalar propagator in which both the Higgs boson h and the flavon H_F propagate.

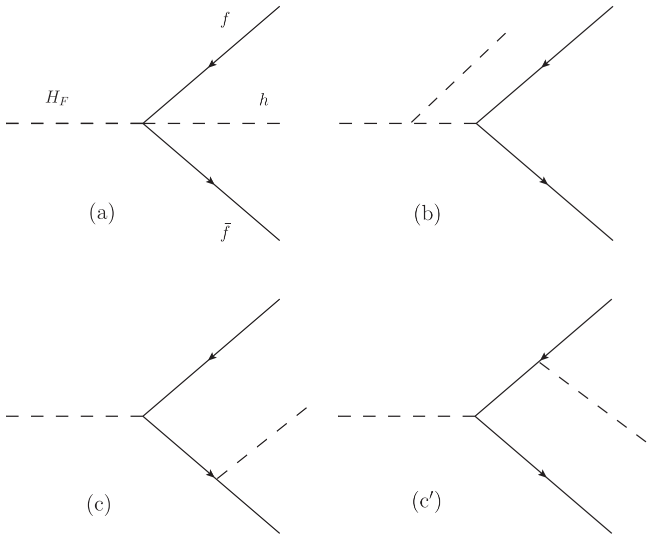

FIG. 1. Feynman diagrams inducing the $H_F \to \bar{f} f h$ decay in the FNSM. (a) shows the direct coupling among H_F, h, and $f\bar{f}$. In (b) the decay goes through an internal scalar line that can be either h or H_F. (c) and (c') show the H_F decaying into $f\bar{f}$ with the h emitted from an internal fermion line.

production signatures and our signal is the resonant effect that offers the decay $H_F \to b\bar{b}h$. This is a great advantage from an experimental point of view.

The paper is organized as follows. Section II presents the relevant aspects of the model, including expressions for the masses and the Feynman rules to be used in the subsequent analysis. Afterward, both theoretical and experimental constraints that have a direct impact on the predictions are studied in Sec. III. Meanwhile, Sec. IV is focused on the analysis of the signal, $pp \to H_F \to hb\bar{b}$ ($h \to b\bar{b}, \gamma\gamma$), as well as its background processes. A multivariate analysis is also included. Finally, we present our conclusions in Sec. V.

II. THE MODEL

A. The scalar sector

The FNSM's scalar sector adds one complex singlet FN scalar S_F to the SM, namely,

$$S_F = \frac{(v_s + S_R + iS_I)}{\sqrt{2}}, \tag{2.1}$$

where v_s represents the vacuum expectation value (VEV) of the FN singlet. The scalar potential is invariant under the FN $U(1)_F$ flavor symmetry. Under this flavor symmetry, S_F and the SM Higgs doublet $\Phi = (\frac{v+\phi^0}{\sqrt{2}} \phi^+)^T$ transform as $S_F \to e^{i\alpha} S_F$ and $\Phi \to \Phi$, respectively. We note that such a scalar potential allows a complex VEV, $\langle S_F \rangle_0 = \frac{v_s}{\sqrt{2}} e^{i\alpha}$, but in this work we assume the scenario in which the Higgs potential is CP conserving ($\alpha = 0$). Then, the CP-conserving Higgs potential reads as

$$V_0 = -\frac{1}{2} m_1^2 \Phi^\dagger \Phi - \frac{1}{2} m_2^2 S_F^* S_F + \frac{1}{2} \lambda_1 (\Phi^\dagger \Phi)^2 + \lambda_2 (S_F^* S_F)^2 + \lambda_3 (\Phi^\dagger \Phi)(S_F^* S_F). \tag{2.2}$$

After the spontaneous symmetry breaking of the $U(1)_F$ flavor symmetry by the VEVs of the spin-0 fields (Φ, S_F), a massless Goldstone boson will emerge in the physical spectrum. To give a mass to it, we embed a soft $U(1)_F$ breaking term in the scalar potential:

$$V_{\text{soft}} = -\frac{m_3^2}{2} (S_F^2 + S_F^{*2}). \tag{2.3}$$

Thus, the full scalar potential is given by

$$V = V_0 + V_{\text{soft}}. \tag{2.4}$$

The parameter λ_3 in Eq. (2.2) allows a mixing between the flavon and the Higgs fields after both the $U(1)_F$ flavor and electroweak (EW) symmetries are spontaneously broken, generating the masses of the flavon and Higgs field, as presented below while the pseudoscalar flavon (S_I) mass is generated via the soft $U(1)_F$ flavor symmetry breaking term V_{soft}. Once the minimization of the potential V is done, we obtain relations between the parameters of V as follows:

$$m_1^2 = v^2 \lambda_1 + v_s^2 \lambda_3, \tag{2.5}$$

$$m_2^2 = -2m_3^2 + 2v_s^2 \lambda_2 + v^2 \lambda_3. \tag{2.6}$$

Since all parameters of the scalar potential are assumed to be real, the imaginary and real parts of V do not mix. The CP-even mass matrix can be written in the (ϕ_0, S_R) basis as

$$M_S^2 = \begin{pmatrix} \lambda_1 v^2 & \lambda_3 v v_s \\ \lambda_3 v v_s & 2\lambda_2 v_s^2 \end{pmatrix}, \tag{2.7}$$

whose mass eigenstates can be obtained through the following 2×2 rotation:

$$\phi^0 = \cos\alpha\, h + \sin\alpha\, H_F, \tag{2.8}$$

$$S_R = -\sin\alpha\, h + \cos\alpha\, H_F, \tag{2.9}$$

where α is the mixing angle. We identify h with the SM-like Higgs boson with mass $M_h = 125.5$ GeV. Meanwhile, the mass eigenstate H_F is identified with the CP-even flavon. The CP-odd flavon $A_F \equiv S_I$ will obtain its mass from the V_{soft} term such that $M_{A_F}^2 = 2m_3^2$. We will work (as free parameters) with the physical masses $M_S (S = h, H_F, A_F)$ and the mixing angle α, whose relations with the quartic couplings of the scalar potential in Eq. (2.2) read as

$$\lambda_1 = \frac{\cos\,\alpha^2 M_h^2 + \sin\,\alpha^2 M_{H_F}^2}{v^2},$$
$$\lambda_2 = \frac{M_{A_F}^2 + \cos\,\alpha^2 M_{H_F}^2 + \sin\,\alpha^2 M_h^2}{2v_s^2},$$
$$\lambda_3 = \frac{\cos\,\alpha\,\sin\,\alpha}{v v_s}(M_{H_F}^2 - M_h^2). \tag{2.10}$$

B. The Yukawa sector

The effective $U(1)_F$ invariant Yukawa Lagrangian includes terms that become the Yukawa couplings after the $U(1)_F$ flavor symmetry is spontaneously broken. It is given by [8]

$$\mathcal{L}_Y = \rho_{ij}^d \left(\frac{S_F}{\Lambda}\right)^{q_{ij}^d} \bar{Q}_i d_j \tilde{\Phi} + \rho_{ij}^u \left(\frac{S_F}{\Lambda}\right)^{q_{ij}^u} \bar{Q}_i u_j \Phi + \rho_{ij}^\ell \left(\frac{S_F}{\Lambda}\right)^{q_{ij}^l} \bar{L}_i \ell_j \Phi + \text{H.c.}, \tag{2.11}$$

where ρ_{ij}^f ($f = u, d, \ell$) are dimensionless parameters ostensibly of order $\mathcal{O}(1)$. The amounts q_{ij}^f represent the Abelian charges that reproduce the observed fermion masses, and Λ is the ultraviolet mass scale, which is not predicted by the Froggat-Nielssen mechanism, it can be between the weak and the Planck scale. However, there is an essential requirement: the flavor symmetry must be broken in such a way that the ratio $\frac{v_s}{\sqrt{2}\Lambda} \lesssim 1$. To generate the Yukawa couplings from Lagrangian (2.11) one must spontaneously break both, the $U(1)_F$ as well as EW symmetries. Once this is done, we arrive at the $Sf_i\bar{f}_i$ interactions as shown in Table I. We note that to avoid large deviations from the SM coupling, $v_s \approx \Lambda$ and $\cos\alpha \approx -1$ are required, as below.

The CP-even H_F and the CP-odd A_F flavons are assumed to be heavier than h.

TABLE I. Diagonal SXX interactions, ($S = h, H_F, A_F$).

Vertex SXX	Coupling
$hf_i\bar{f}_i$	$\frac{v_s m_f}{v\Lambda^2}(v\sin\alpha - v_s\cos\alpha)$
hZZ	$g\frac{m_Z}{c_W}\cos\alpha$
hWW	$gm_W\cos\alpha$
$H_F f_i\bar{f}_i$	$-\frac{v_s m_f}{v\Lambda^2}(v_s\sin\alpha + v\cos\alpha)$
$H_F ZZ$	$g\frac{m_Z}{c_W}\sin\alpha$
$H_F WW$	$gm_W\sin\alpha$
$A_F f_i\bar{f}_i$	$-\frac{v_s m_f}{\Lambda^2}$
$A_F ZZ$	0
$A_F WW$	0

Meanwhile, to induce nondiagonal $Sf_i\bar{f}_j$ interactions, we proceed as described below. By considering the unitary gauge one can make the following first order expansion of the neutral component of the heavy flavon field S_F around its VEV v_s:

$$\left(\frac{S_F}{\Lambda}\right)^{q_{ij}} = \left(\frac{v_s + S_R + iS_I}{\sqrt{2}\Lambda}\right)^{q_{ij}} \simeq \left(\frac{v_s}{\sqrt{2}\Lambda}\right)^{q_{ij}} \left[1 + q_{ij}\left(\frac{S_R + iS_I}{v_s}\right)\right], \tag{2.12}$$

which leads to the following Lagrangian interaction after replacing the mass eigenstates:

$$\mathcal{L}_Y = \frac{1}{v}[\bar{U}M^u U + \bar{D}M^d D + \bar{L}M^\ell L](c_\alpha h + s_\alpha H_F) + \frac{v}{\sqrt{2}v_s}[\bar{U}_i \tilde{Z}_{ij}^u U_j + \bar{D}_i \tilde{Z}_{ij}^d D_j + \bar{L}_i \tilde{Z}_{ij}^\ell L_j] \times (-\sin\,\alpha h + \cos\,\alpha H_F + iA_F) + \text{H.c.} \tag{2.13}$$

Here, M^f denotes the diagonal fermion mass matrix. We encapsulate the Higgs-flavon couplings in the $\tilde{Z}_{ij}^f = U_L^f Z_{ij}^f U_L^{f\dagger}$ matrices. In the flavor basis, the Z_{ij}^f matrix elements are given by

$$Z_{ij}^f = \rho_{ij}^f \left(\frac{v_s}{\sqrt{2}\Lambda}\right)^{q_{ij}^f} q_{ij}^f, \tag{2.14}$$

which (in general) remains nondiagonal even after diagonalizing the mass matrices, giving rise to flavor violating interactions.

Finally, in addition to the Yukawa couplings, we also need the $H_F h f_i \bar{f}_j$ couplings for our calculations. In the FNSM these interactions are given by

$$H_F h f\bar{f} = \frac{m_f v_s}{\sqrt{2}\Lambda^2}(1 - 2\cos^2\alpha). \tag{2.15}$$

As a particular case we will explore the scenario where $f = b$. This choice is motivated by experimental reports on Higgs pair searches [3–7].

III. CONSTRAINTS ON THE FNSM PARAMETER SPACE

In order to compute a realistic numerical analysis of the signals proposed in this project, i.e., $pp \to H_F \to hb\bar{b}$ ($h \to b\bar{b}, \tau^-\tau^+, WW^*, \gamma\gamma, ZZ^*$), we need to constrain the free FNSM parameters involved in the upcoming calculations, namely,

(1) The mixing angle α of the real components of the doublet Φ and the FN singlet S.
(2) FN singlet VEV v_s.
(3) The ultraviolet mass scale Λ.
(4) CP-even scalar mass M_{H_F}.

These parameters can be constrained by several types of theoretical restrictions like absolute vacuum stability, triviality, perturbativity, and unitarity of scattering matrices and different experimental data, mainly, LHC Higgs boson data upper limits on the production cross section of additional Higgs states. We also consider bounds on lepton flavor violating processes (LFVp) $L_i \to \ell_j \ell_k \overline{\ell}_k$, $\ell_i \to \ell_j \gamma$. Measurements on $\mathcal{BR}(B^0_{s,d} \to \mu^+\mu^-)$ and the anomalous magnetic moments of the muon and electron Δa_μ and Δa_e, respectively, are also presented. Finally, we also take into account quark flavor constraints: $B-\bar{B}$, $K-\bar{K}$, and $D-\bar{D}$ mixing.

A. Theoretical constraints

1. Stability of the scalar potential

It is necessary to control the stability of the scalar potential in Eq. (2.2); it should be bounded from below, i.e., it should not approach negative infinity along any direction of the field space (h, H_F, A_F) at large field values. The quadratic terms in the scalar potential are very suppressed compared to the quartic terms. So, the absolute stability conditions read [14] as

$$(\lambda_1, \lambda_2, \lambda_3 + \sqrt{2\lambda_1\lambda_2}) > 0. \tag{3.1}$$

The quartic couplings are evaluated at a scale Λ using the renormalization group evolution (RGE) equations. If the scalar potential in Eq. (2.2) has a metastable EW vacuum, then these conditions should be modified [14]. To constrain the scalar field masses M_ϕ, the VEV of the complex singlet v_s and the mixing angle α, we can use Eq. (2.10) to translate these limits into those on the model parameters.

2. Perturbativity and unitarity constraints

The upper limits presented in Eq. (3.2) are necessary to ensure that the radiatively corrected scalar potential of the FNSM remains perturbative at any energy scale:

$$|\lambda_1, \lambda_2, \lambda_3| \leq 4\pi. \tag{3.2}$$

The quartic couplings that come from the scalar potential are also highly constrained by the unitarity of the S matrix. Even at large field values, one can obtain the S matrix by considering several $(P)S-(P)S$, $V-V$, and $(P)S-V$ interactions in $2 \to 2$ body processes, where $P(S,V)$ stands for a pseudoscalar boson (scalar, gauge boson). The unitarity of the S matrix demands that its eigenvalues be less than 8π [14,15]. Within the theoretical framework of FNSM, using the equivalence theorem, the unitary bounds are given by

$$\lambda_1 \leq 16\pi \quad \text{and}$$

$$|\lambda_1 + \lambda_2 \pm \sqrt{(\lambda_1 - \lambda_2)^2 + (2/3\lambda_3)^2}| \equiv |\lambda_U^\pm| \leq 16/3\pi. \tag{3.3}$$

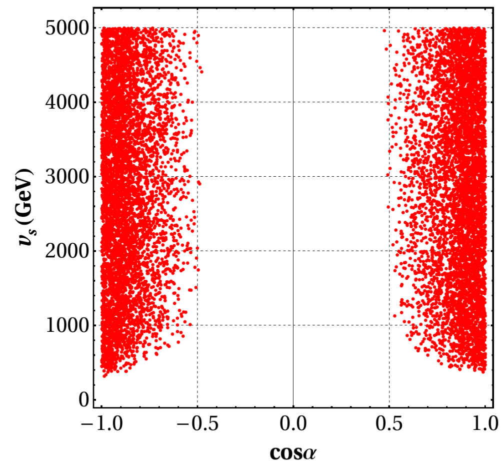

FIG. 2. VEV of the FN singlet v_s as a function of cosine of the mixing angle α. The red points indicate those allowed by all theoretical restrictions as mentioned in the main text.

By using Eqs. (2.10), (3.2), and (3.3), we can constrain the scalar singlet VEV v_s, the heavy Higgs masses (M_{H_F}, M_{A_F}), and the mixing angle α.

Figure 2 displays the $\cos\alpha - v_s$ plane whose points represent those allowed by the theoretical constraints, perturbativity, and unitarity of the S matrix. For this purpose we generate random points such that they meet the relations (2.10), (3.2), and (3.3). We present in Table II the scanned intervals to achieve that proposal.

We find that $|\lambda_U^+| \leq 16\pi/3$ is the most stringent upper bound for the scalar quartic couplings, which is transferred to a lower limit on the scalar singlet VEV $v_s \geq (276, 345, 415, 519)$ GeV, for specific masses of $M_{H_F} = M_{A_F} = (800, 1000, 1200, 1500)$ GeV and $\cos\alpha = -0.995$. Note that we are working at the EW scale only, as detailed RGE analysis is beyond the scope of this work. We also observe a greater density around 1 and -1; this is because α must tend to zero so as not to have large deviations from the $hf\bar{f}$ coupling of the SM.

It is important to highlight that the masses were analyzed in the range shown in Table II because in a previous study by one of us (and others) [11], it was found that $M_{H_F} > 800$ GeV to release the limit on the cross section of the process $pp \to S \to hh$ reported by the ATLAS Collaboration [16], where S is a resonant (pseudo)scalar particle.

TABLE II. Scanned parameters.

Parameter	Interval
$\cos\alpha$	$[-1, 1]$
M_{H_F}	800–1500 GeV
M_{A_F}	800–1500 GeV
v_s	$v - 5000$ GeV

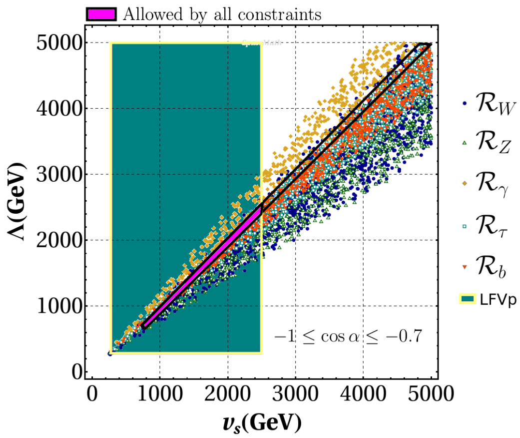

FIG. 3. Ultraviolet mass scale Λ as a function of the VEV of the complex singlet v_s. The different points represent individual $\mathcal{R}'_X s$, while the enclosed area by solid black lines is the common zone of them. The green rectangle stands for the allowed region by LFVp. Meanwhile, the cyan area is the result of applying all discussed theoretical and experimental constraints (intersection).

B. Experimental constraints

1. LHC Higgs boson data

We complement the theoretical constraints by using experimental measurements of Higgs boson physics [17]; specifically we consider the *signal strengths* defined as

$$\mathcal{R}_X = \frac{\sigma(pp \to h) \cdot \mathcal{BR}(h \to X)}{\sigma(pp \to h^{\rm SM}) \cdot \mathcal{BR}(h^{\rm SM} \to X)}, \qquad (3.4)$$

where $\sigma(pp \to H_i)$ is the production cross section of H_i, with $H_i = h, h^{\rm SM}$; here h is the SM-like Higgs boson coming from an extension of the SM and $h^{\rm SM}$ is the SM Higgs boson; $\mathcal{BR}(H_i \to X)$ is the branching ratio of the decay $H_i \to X$, with $X = b\bar{b}, c\bar{c}, \tau^-\tau^+, \mu^-\mu^+, WW^*, ZZ^*, \gamma\gamma$.

2. Lepton flavor violating processes

Furthermore, we also analyze several LFVp that can help us even more in constraining the parameters involved in subsequent calculations. Specifically, we use (i) upper limits on $\mathcal{BR}(L_i \to \ell_j \ell_k \bar{\ell}_k)$ and $\mathcal{BR}(\ell_i \to \ell_j \gamma)$, (ii) measurements on $\mathcal{BR}(B^0_{s,d} \to \mu^+\mu^-)$ and the anomalous magnetic moments of the muon Δa_μ. We also analyze the upper limit on $\mathcal{BR}(h \to \ell_i \ell_j)$ [18,19]. However, we find it is not restricted enough. We implement the model in the *Mathematica* package, so-called SpaceMath [20], to analyze the FNSM parameter space. We present in Fig. 3 the ultraviolet mass scale Λ as a function of the VEV of the complex singlet v_s. The different points represent individual $\mathcal{R}'_X s$; the blue circles (green triangles, yellow diamonds, green squares, orange triangles, green rectangles) correspond to $\mathcal{R}_W$ ($\mathcal{R}_Z, \mathcal{R}_\gamma, \mathcal{R}_\tau, \mathcal{R}_b$). The common region of all them is represented by the enclosed area in solid black lines. The green rectangle stands for the allowed area by all the LFVp.[2] Meanwhile, the cyan area is the result of applying all discussed theoretical and experimental constraints (intersection). Motivated by the analysis done in Sec. III A 2, we again scan the model's parameters involved in the evaluation of the $\mathcal{R}_X$'s, as shown in Table III. We also have explored the allowed values by $\mathcal{R}_{\mu,c}$ (not presented in Fig. 3); however, these measurements are not very stringent in the FNSM. It is worth highlighting the fact that $v_s \approx \Lambda$; this is to be expected because the coupling $hf\bar{f}$ behaves as v_s^2/Λ^2 for $\cos\alpha \approx -1$, as shown in Table I.

TABLE III. Scanned parameters.

Parameter	Interval
$\cos\alpha$	$[-1, -0.7]$
Λ	$v - 5000$ GeV
v_s	$v - 5000$ GeV

3. Neutral meson mixing

The effective Hamiltonian describing $\Delta F = 2$ interactions is given by

$$\begin{aligned}\mathcal{H}_{\rm eff}^{\Delta F=2} = {}& C_1^{ij}(\bar{q}_L^i \gamma_\mu q_L^j)^2 + \tilde{C}_1^{ij}(\bar{q}_R^i \gamma_\mu q_R^j)^2 + C_2^{ij}(\bar{q}_R^i q_L^j)^2 \\ &+ \tilde{C}_2^{ij}(\bar{q}_L^i q_R^j)^2 + C_4^{ij}(\bar{q}_R^i q_L^j)(\bar{q}_L^i q_R^j) \\ &+ C_5^{ij}(\bar{q}_L^i \gamma_\mu q_L^j)(\bar{q}_R^i \gamma^\mu q_R^j) + \text{H.c.} \end{aligned} \qquad (3.5)$$

At tree level, flavon exchange leads to the generation of Wilson coefficients [21,22]

$$\begin{aligned} C_2^{ij} &= -(g_{ji}^*)^2 \left(\frac{1}{m_s^2} - \frac{1}{m_a^2}\right) \\ \tilde{C}_2^{ij} &= -g_{ij}^2 \left(\frac{1}{m_s^2} - \frac{1}{m_a^2}\right) \\ C_4^{ij} &= -\frac{g_{ij} g_{ji}}{2} \left(\frac{1}{m_s^2} + \frac{1}{m_a^2}\right). \end{aligned} \qquad (3.6)$$

For $M_{A_F} = M_{H_F}$ the two contributions to C_2 and $\tilde{C}_2$ cancel, whereas constructive interference can be generated via the Wilson coefficient C_4.

4. $K - \bar{K}$ mixing

The limits from $K - \bar{K}$ mixing at 95% CL [23] are given by

[2]According to our analysis, the upper bound on Λ and v_s is imposed by the anomalous magnetic moment of the muon. However, the situation could change because it is still possible that more precise determinations of the SM hadronic contribution and the experimental measurement would settle the discrepancy in the future without requiring any new physics effects.

$$C_{\epsilon_K} = \frac{\mathrm{Im}\langle K^0|\mathcal{H}^{\Delta F=2}|\bar{K}^0\rangle}{\mathrm{Im}\langle K^0|\mathcal{H}^{\Delta F=2}_{\mathrm{SM}}|\bar{K}^0\rangle} = 1.12^{+0.27}_{-0.25};$$
$$C_{\Delta m_K} = \frac{\mathrm{Re}\langle K^0|\mathcal{H}^{\Delta F=2}|\bar{K}^0\rangle}{\mathrm{Re}\langle K^0|\mathcal{H}^{\Delta F=2}_{\mathrm{SM}}|\bar{K}^0\rangle} = 0.93^{+1.14}_{-0.42}.$$

The contributions of SM and flavon are included in $\mathcal{H}^{\Delta F=2}$, while $\mathcal{H}^{\Delta F=2}_{\mathrm{SM}}$ represents the contribution of SM. The observed dip characteristic arises from the accidental cancellation that occurs in C_2^{sd} and $\tilde{C}_2^{sd}$, as shown in the Wilson coefficients generated by flavon exchange at tree level [21,22]. This feature is universally observed within $K-\bar{K}$ mixing. However, it is absent in the specific scenarios where the contribution to C_4^{sd} becomes so dominant that it overshadows all other contributions.

5. $B-\bar{B}$ mixing

For both variations of $B-\bar{B}$ mixing, it is defined as follows:

$$C_{B_q} e^{2i\varphi_{B_q}} = \frac{\langle B_q|\mathcal{H}^{\Delta F=2}|\bar{B}_q\rangle}{\langle B_q|\mathcal{H}^{\Delta F=2}_{\mathrm{SM}}|\bar{B}_q\rangle}, \tag{3.7}$$

with the 95% CL limits [23] given by

$$C_{B_d} = 1.05 \pm 0.11, \qquad \varphi_{B_d} = -2.0 \pm 1.8,$$
$$C_{B_s} = 1.110 \pm 0.090, \qquad \varphi_{B_s} = 0.42 \pm 0.89. \tag{3.8}$$

6. $D-\bar{D}$ mixing

Given that the SM contribution to the $D-\bar{D}$ mixing process is significantly affected by substantial hadronic uncertainties, it is recommended to define and restrict the contributions of flavons ensuring that they do not exceed the constraint 2σ [24]:

$$|M_{12}^D| = |\langle D|\mathcal{H}^{\Delta F=2}|\bar{D}\rangle < 7.5\times 10^{-3}\ \mathrm{ps}^{-1}. \tag{3.9}$$

In Refs. [9,25] stringent restrictions are presented in the $v_s - M_{A_F}$ plane that come from mixtures of mesons. However, we evade them by inheriting them to the parameters $\tilde{Z}_{ds}$, $\tilde{Z}_{db}$, and $\tilde{Z}_{uc}$ for $K-\bar{K}$, $B-\bar{B}$, and $D-\bar{D}$, respectively. We presented in Fig. 4 the $M_{H_F} - v_s$ plane for three different values of $\tilde{Z}_{uc}$: 10^{-10}, 10^{-9}, and 5×10^{-9}. The colored areas are those allowed by $|M_{12}^D|$. Similar constraints are obtained for $K-\bar{K}$ and $B-\bar{B}$.

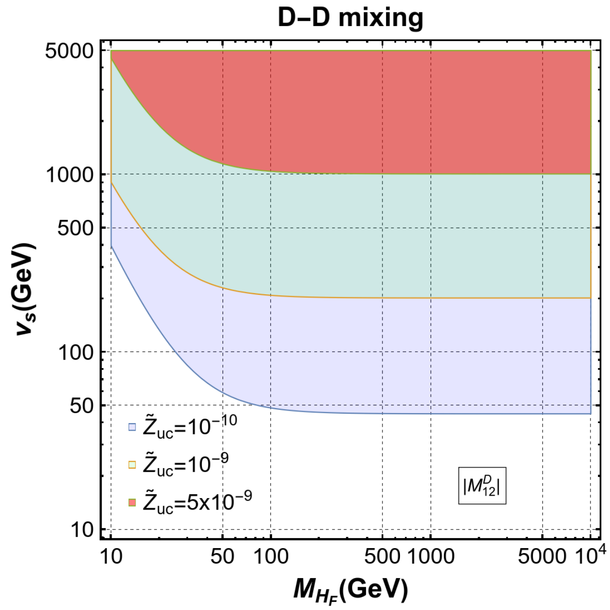

FIG. 4. $M_{H_F} - v_s$ plane showing the region allowed due to flavon contributions to $|M_{12}^D|$. Blue area: $\tilde{Z}_{uc} = 10^{-10}$, green area: $\tilde{Z}_{uc} = 10^{-9}$, red area: $\tilde{Z}_{uc} = 5\times 10^{-9}$.

IV. COLLIDER ANALYSIS

We first present the decay width $\Gamma(H_F \to h\bar{f}f)$ of the three-body process in which we are interested. The study of these kinds of processes is interesting as it can also have a sizable branching ratio. The Feynman diagrams that contribute to these reactions are shown in Fig. 1.

The decay width can be written as follows:

$$\Gamma(H_F \to h\bar{f}f) = \frac{M_{H_F}}{256\pi^3}\int dx_a \int dx_b |\bar{\mathcal{M}}|^2, \tag{4.1}$$

where the average square amplitude is given by

$$\begin{aligned}
|\bar{\mathcal{M}}|^2 =& \frac{1}{2(x_a+x_b+x_h-2)^2}(x_a+x_b+x_h-4x_t-1)((x_a+x_b+x_h-2)C_a+C_b)^2 \\
&+\frac{2}{(x_a-1)^2(x_b-1)^2}((x_a-1)(x_b-1)(x_a-x_b)^2-16(x_a+x_b-2)^2x_t^2 \\
&+4(x_a+x_b-2)(2-3x_b+x_a(4x_b-3))x_t+x_h(4(x_a+x_b-2)^2x_t-(x_a-x_b)^2))C_c^2 \\
&-\frac{4\sqrt{x_t}}{(x_a-1)(x_b-1)}(x_a^2+2(3x_b+x_h-4x_t-3)x_a+x_b^2-4x_h+2x_b(x_h-4x_t-3)+16x_t+4)C_aC_c \\
&-\frac{4\sqrt{x_t}}{(x_a-1)(x_b-1)(x_a+x_b+x_h-2)}(x_a^2+2(3x_b+x_h-4x_t-3)x_a+x_b^2-4x_h+2x_b(x_h-4x_t-3)+16x_t+4)C_bC_c,
\end{aligned} \tag{4.2}$$

with $x_a = (m_a/M_{H_F})^2$. The factors $C_a = g_{H_F hff}$, $C_b = g_{H_F hh} g_{hff}/m_h^2$, and $C_c = g_{H_F ff} g_{hff}/m_h$ are the coupling constants involved in the Feynman diagrams of Fig. 1. Finally, the integration domain is given by

$$2\sqrt{x_t} \leq x_a \leq 1 - x_h - 2\sqrt{x_t x_h}, \tag{4.3}$$

$$x_b \gtreqless \frac{2(1 - x_h + 2x_t) + x_a(x_a + x_h - 2x_t - 3) \mp \sqrt{x_a^2 - 4x_t}\sqrt{(x_a + x_h - 1)^2 - 4x_h x_t}}{2(1 - x_a + x_t,)}. \tag{4.4}$$

Meanwhile, the production cross section of the heavy CP-even flavon H_F (or pseudoscalar A_F, for that matter) depends mainly on the $g_{H_F t\bar{t}} = \frac{c_\alpha v + s_\alpha v_s}{v_s} \frac{y_t}{\sqrt{2}}$ ($g_{A_F t\bar{t}} = \frac{v}{v_s} \frac{y_t}{\sqrt{2}}$) coupling. The corresponding term in the effective Lagrangian reads [26] as

$$\mathcal{L}_{\text{eff}} = \frac{1}{v} g_{hgg} h G_{\mu\nu} G^{\mu\nu}, \tag{4.5}$$

$$g_{Sgg} = -i \frac{\alpha_S}{8\pi} \tau(1 + (1 - \tau) f(\tau)) \quad \text{with} \quad \tau = \frac{4M_t^2}{M_h^2}, \tag{4.6}$$

$$f(\tau) = \begin{cases} \left(\sin^{-1}\sqrt{\frac{1}{\tau}}\right)^2, & \tau \geq 1, \\ -\frac{1}{4}\left[\ln \frac{1+\sqrt{1-\tau}}{1-\sqrt{1-\tau}} - i\pi\right]^2 & \tau < 1. \end{cases} \tag{4.7}$$

In FNSM, the ggh, ggH_F, and ggA_F couplings are given, respectively, by

$$\begin{aligned} g_{hgg} &= \left(\frac{c_\alpha v_s - s_\alpha v}{v_s}\right) g_{Sgg}, \\ g_{H_F gg} &= \left(\frac{c_\alpha v + s_\alpha v_s}{v_s}\right) g_{Sgg}, \\ g_{A_F gg} &= \frac{v}{v_s}(-i\alpha_S/\pi)\tau f(\tau). \end{aligned} \tag{4.8}$$

A_F is a CP-odd scalar, and h, H_F, are CP-even scalars, so, once the couplings with left and right fields are written in terms of Dirac fields, the Hermitian part of the coupling in Eq. (2.11) gives rise to an $i = \sqrt{-1}$ coupling for h, H_F, and a γ_5 coupling for A_F: so the result of the top quark loop integral is different for h, H_F, and A_F [27,28]. It is to be noted that, for $M_{H_F, A_F} > 2M_t$, $f(\tau) = -\frac{1}{4}[\ln \frac{1+\sqrt{1-\tau}}{1-\sqrt{1-\tau}} - i\pi]^2$.

As far as our computation scheme is concerned, we first use FeynRules [29] to obtain the FNSM model and produce the UFO files for MadGraph-2.6.5 [30]. Using the ensuing particle spectrum in MadGraph-2.6.5, we calculate the production cross section of the aforementioned production and decay process. The MadGraph_aMC@NLO [30] framework has been used to generate the background events in the SM. The showering and hadronization simulations were performed with Pythia-8 [31]. The detector response has been emulated using DELPHES-3.4.2 [32]. The default ATLAS card which comes along with the DELPHES-3.4.2 package was considered in this analysis. For both the signal and background processes, we consider the leading order cross sections computed by MadGraph_aMC@NLO.

Once we have put on the table the way in which we evaluate the collider observables, we define in Table IV three scenarios to be studied in the following analysis.

We present in Table V the numerical cross section of the proposed signal and the number of events produced by considering scenarios **S1**, **S2**, and **S3**.

Meanwhile, Fig. 5 presents an overview of the production cross section of the signal $pp \to H_F \to hb\bar{b}$ by considering the three scenarios, **S1**, **S2**, and **S3**.

On the other hand, we analyze two particular channels in which the Higgs boson decays, namely, (i) $pp \to H_F \to hb\bar{b}(h \to b\bar{b})$ and (ii) $pp \to H_F \to hb\bar{b}(h \to \gamma\gamma)$. The b tagging of jets produced from the fragmentation and hadronization of bottom quarks represents a fundamental role in separating the signal from the background processes, which involve gluons, light-flavor jets (u, d, s), and c-quark fragmentation. To overcome this problem, we use the FastJet package [33] (via MadAnalysis [34]) and invoke the anti-k_T algorithm [35]. We also include the b-tagging efficiency $\epsilon_b = 90\%$. The probability that a $c-$jet or

TABLE IV. Scenarios (**S1**, **S2**, **S3**) used in the calculations.

Parameter	**S1**	**S2**	**S3**
$\cos\alpha$	0.995	0.995	0.995
Λ	1 TeV	1.5 TeV	2.5 TeV
v_s	1 TeV	1.5 TeV	2.5 TeV

TABLE V. Cross section of the signal for scenarios **S1**, **S2**, **S3**.

Scenario	M_{H_F} (GeV)	$\sigma(pp \to H_F \to hb\bar{b})$ (fb)	Events ($\mathcal{L}_{\text{int}} = 300\,\text{fb}^{-1}$)
S1	(800, 900, 1000)	(6.8, 3.3, 1.7)	(2040, 990, 510)
S2	(800, 900, 1000)	(4.3, 2.3, 1.3)	(1290, 690, 390)
S3	(800, 900, 1000)	(3.8, 2.1, 1.1)	(1140, 630, 330)

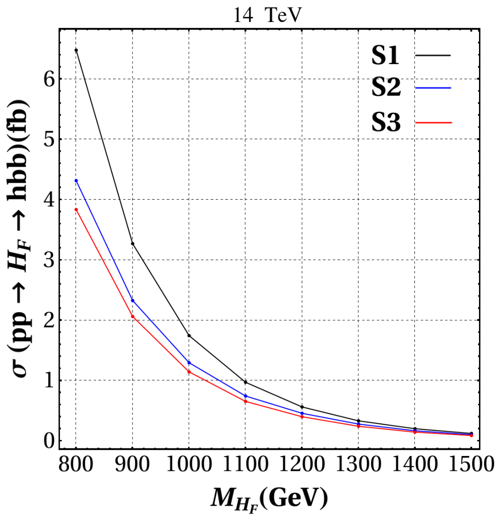

FIG. 5. Production cross section of the signal $pp \to H_F \to hb\bar{b}$. The center-of-mass energy was set to 14 TeV.

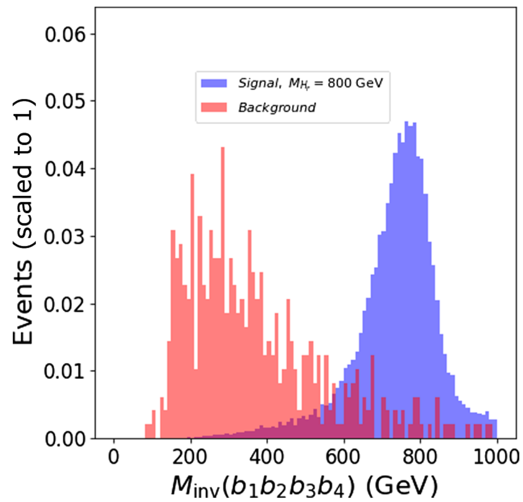

FIG. 6. Normalized distribution of the reconstructed invariant mass $M_{\rm inv}(b_1b_2b_3b_4)$ for the signal and background processes.

any other light-jet j is mistagged as a $b-$jet is $\epsilon_c = 5\%$ and $\epsilon_j = 1\%$ [36], respectively.

A. $pp \to H_F \to hb\bar{b}(h \to b\bar{b})$

The SM background processes for the $h \to b\bar{b}$ channel are given by

(1) $pp \to t\bar{t}$, $(t \to W^+\bar{b}, W^+ \to c\bar{b}, \bar{t} \to W^-b, W^+ \to b\bar{c})$.
(2) $pp \to Wh$, $(W \to cb, h \to b\bar{b})$.
(3) $pp \to ZZ$, $(Z \to b\bar{b}, Z \to b\bar{b})$.
(4) $pp \to Zh$, $(Z \to b\bar{b}, h \to b\bar{b})$.
(5) $pp \to b\bar{b}jj$, where j denotes non-bottom-quark jets.

The numerical cross section of the SM background processes is presented in Table VI.

For this channel, the b jets emerging from the primary vertex are expected to have a high transverse momentum $p_T(b_1, b_2)$, while those produced via the decay $h \to b\bar{b}$ have a lower transverse momentum than the primary ones, $p_T(b_3, b_4)$. An important fact, and the clearest signature of our signal, is the resonant effect coming from the decay $H_F \to hb\bar{b}(h \to b\bar{b}) \to b\bar{b}b\bar{b}$.

We present in Fig. 6 the invariant mass $M_{\rm inv}(b_1b_2b_3b_4)$ for scenario $S1$ and $M_{H_F} = 800$ GeV.

Meanwhile, Fig. 7 shows the $p_T(b_i)$ $(i = 1, 2, 3, 4)$ distribution including to the signal and the SM background processes. Subscript 1(4) corresponds to the b jet with the highest (lowest) transverse momentum, while subscript 2(3) represents the second (third) dominant b jet.

TABLE VI. Cross section of the SM background processes.

SM background process	Cross section (fb)
$pp \to t\bar{t}$	26910
$pp \to Wh$	0.5463
$pp \to ZZ$	231.5
$pp \to Zh$	79.75
$pp \to \bar{b}bjj$	5.441×10^8

From Fig. 7 we note that $p_T(b_1, b_2)$ are higher than $p_T(b_3, b_4)$ because the former come from the primary vertex, while the latter arise from the Higgs boson decay. Both $p_T(b_i)$ and $M_{\rm inv}(b_1b_2b_3b_4)$ are the most important variables to isolate the signal from the background.

B. $pp \to H_F \to hb\bar{b}(h \to \gamma\gamma)$

As far as the diphoton channel is concerned, the SM background processes are given by

(1) $pp \to ht\bar{t}$, $(h \to \gamma\gamma, t \to W^+\bar{b}, W^+ \to \ell^+\nu_\ell, \bar{t} \to W^-b, W^+ \to \ell^-\bar{\nu}_\ell)$.
(2) $pp \to t\bar{t}\gamma\gamma$, $(t \to W^+\bar{b}, W^+ \to \ell^+\nu_\ell, \bar{t} \to W^-b, W^+ \to \ell^-\bar{\nu}_\ell)$.
(3) $pp \to Wh$, $(W \to cb, h \to \gamma\gamma)$.
(4) $pp \to Zh$, $(Z \to b\bar{b}, h \to \gamma\gamma)$.
(5) $pp \to hjj$, $(h \to \gamma\gamma)$.
(6) $pp \to \gamma\gamma jj$.
(7) $pp \to \gamma\gamma b\bar{b}$.

The numerical cross section of the SM background processes is presented in Table VII.

In this case we also have a similar scenario as in the previous channel concerning the resonant effect coming from the decay $H_F \to b\bar{b}\gamma\gamma$. Figure 8 displays the invariant mass distribution $M_{\rm inv}(bb\gamma\gamma)$ for $M_{H_F} = 900$ GeV. As in the previous channel, we also present in Fig. 9 the $p_T(b_i)$, $p_T(\gamma_i)$ $(i = 1, 2)$.

C. Multivariate analysis

After the kinematic analysis, we found that most of the observables used to distinguish signal from background have relatively weak discriminating power. Therefore, the final candidate selection is determined using multivariate analysis (MVA) discriminators, which combine these

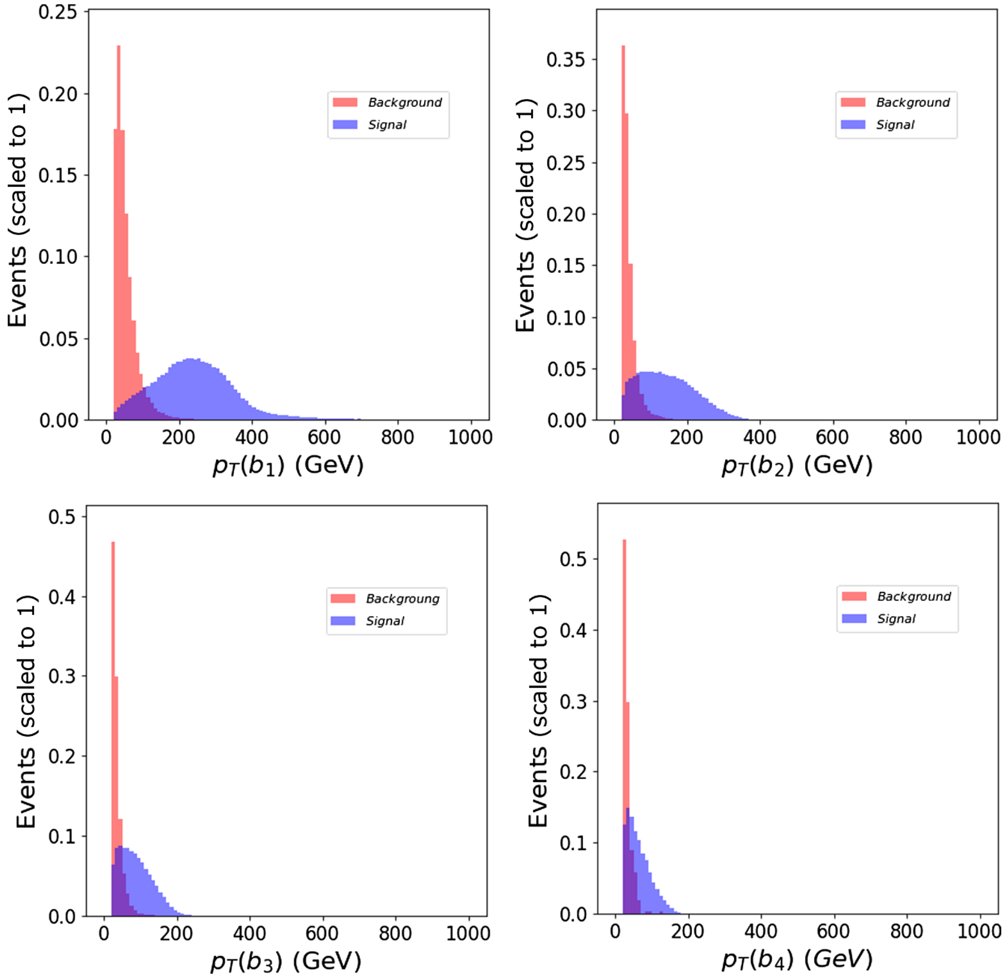

FIG. 7. Normalized distributions in b-jet transverse momentum for signal and total background after the acceptance cuts.

observables into a single, more powerful classifier. For the MVA training, we use a boosted decision tree (BDT) algorithm [37], implemented via the XGBoost library [38], which employs an advanced gradient boosting technique. The BDT classifiers are trained using variables related to the kinematics of final and intermediate state particles, including the following:

Case 1: Four b jets (b_1, b_2, b_3, b_4):

(1) Transverse momentum (p_T): $p_T(b_1)$, $p_T(b_2)$, $p_T(b_3)$, $p_T(b_4)$.

TABLE VII. Cross section of the SM background processes.

SM background processes	Cross section (fb)
$pp \to ht\bar{t}$	3.2×10^{-2}
$pp \to t\bar{t}\gamma\gamma$	0.57
$pp \to Wh$	9.7×10^{-4}
$pp \to Zh$	0.14
$pp \to hjj$	13.62
$pp \to \gamma\gamma jj$	1.1×10^5
$pp \to b\bar{b}\gamma\gamma$	5113

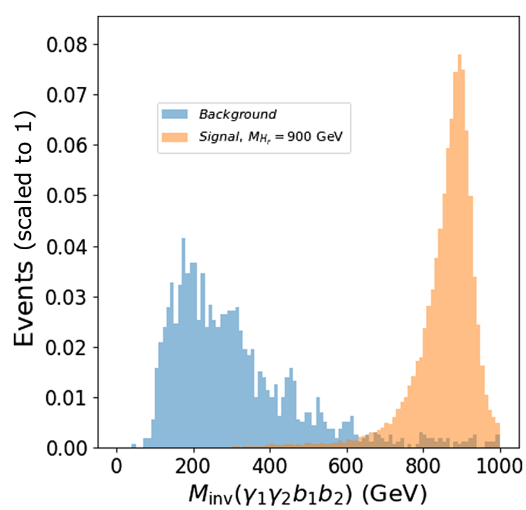

FIG. 8. Normalized distribution of the reconstructed invariant mass $M_{\mathrm{inv}}(\gamma_1\gamma_2 b_1 b_2)$ for the signal and background processes.

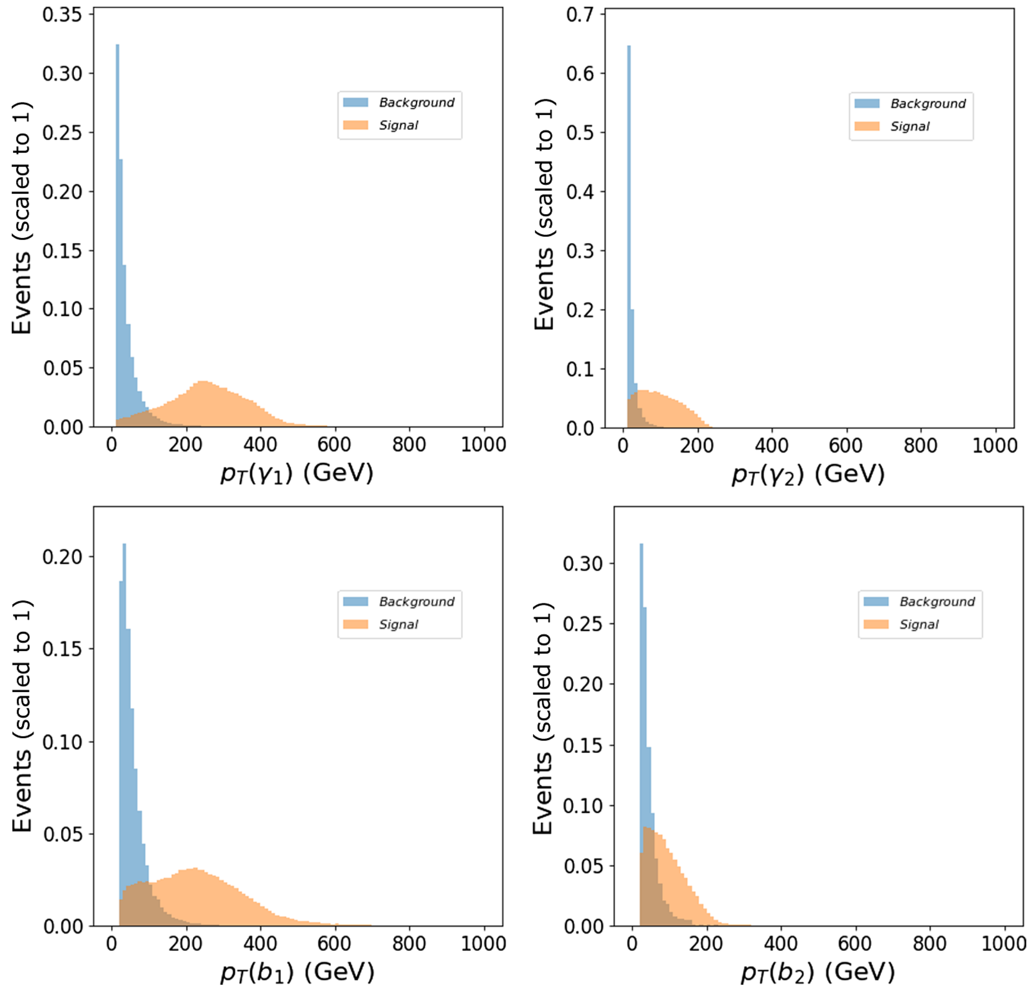

FIG. 9. Normalized distributions in b-jet and γ transverse momentum for signal and total background after the acceptance cuts.

(2) Rapidity (η): $\eta(b_1)$, $\eta(b_2)$, $\eta(b_3)$, $\eta(b_4)$.
(3) Combined transverse momentum: $p_T(b_1 b_2 b_3 b_4)$.

Case 2: Two b jets (b_1, b_2) and two photons (γ_1, γ_2):
(1) Transverse momentum (p_T): $p_T(b_1)$, $p_T(b_2)$, $p_T(\gamma_1)$, $p_T(\gamma_2)$.
(2) Rapidity (η): $\eta(b_1)$, $\eta(b_2)$, $\eta(\gamma_1)$, $\eta(\gamma_2)$.
(3) Invariant mass of the photons: $M(\gamma_1\gamma_2)$.
(4) Combined transverse momentum: $p_T(b_1 b_2 b_3 b_4)$.

The BDT training is performed using the MC-simulated samples. The number of MC events are a dataset consisting of 200,000 signal events and the samples of background events described above, each containing 200,000 events. The data are split as follows: the training dataset is 70% of the total events, while the testing dataset is 30% of the total events. To optimize the BDT model, we use *HyperOpt* [39] to tune the hyper-parameters of the classifier. As an example of the performances of the trainings, Fig. 10 shows the plots for 1/background acceptance against the signal acceptance for the $h \to b\bar{b}$ channel.

These signal and background samples are scaled to the expected number of candidates, which is calculated based on the integrated luminosity and cross sections. The BDT selection is optimized individually for each channel to maximize the figure of merit, i.e., the *signal significance*, defined as $S/\sqrt{S+B}$, where S and B represent the number of signal and background candidates, respectively, in the signal region after applying the selection criteria.

In Fig. 11 we show the *signal significance* (for the three scenarios **Si**) as a function of the luminosity and the flavon mass M_{H_F} for the $pp \to H_F \to hb\bar{b}(h \to b\bar{b})$ process. We observe that at a 14 TeV pp collider with an integrated luminosity of 3000 fb^{-1}, strong sensitivity exists for the various choices of M_{H_F}. We found that for the range $800 < M_{H_F} < 950$ GeV a *signal significance* between $3-5.6\sigma$ was obtained. Thus, with the arrival of the future high-luminosity large hadron collider (HL-LHC), the flavon particle could be discovered if the scenario $S1$ is the one chosen by nature. For scenarios **S2** and **S3** there is a depletion around 1.2 TeV, and then the significance

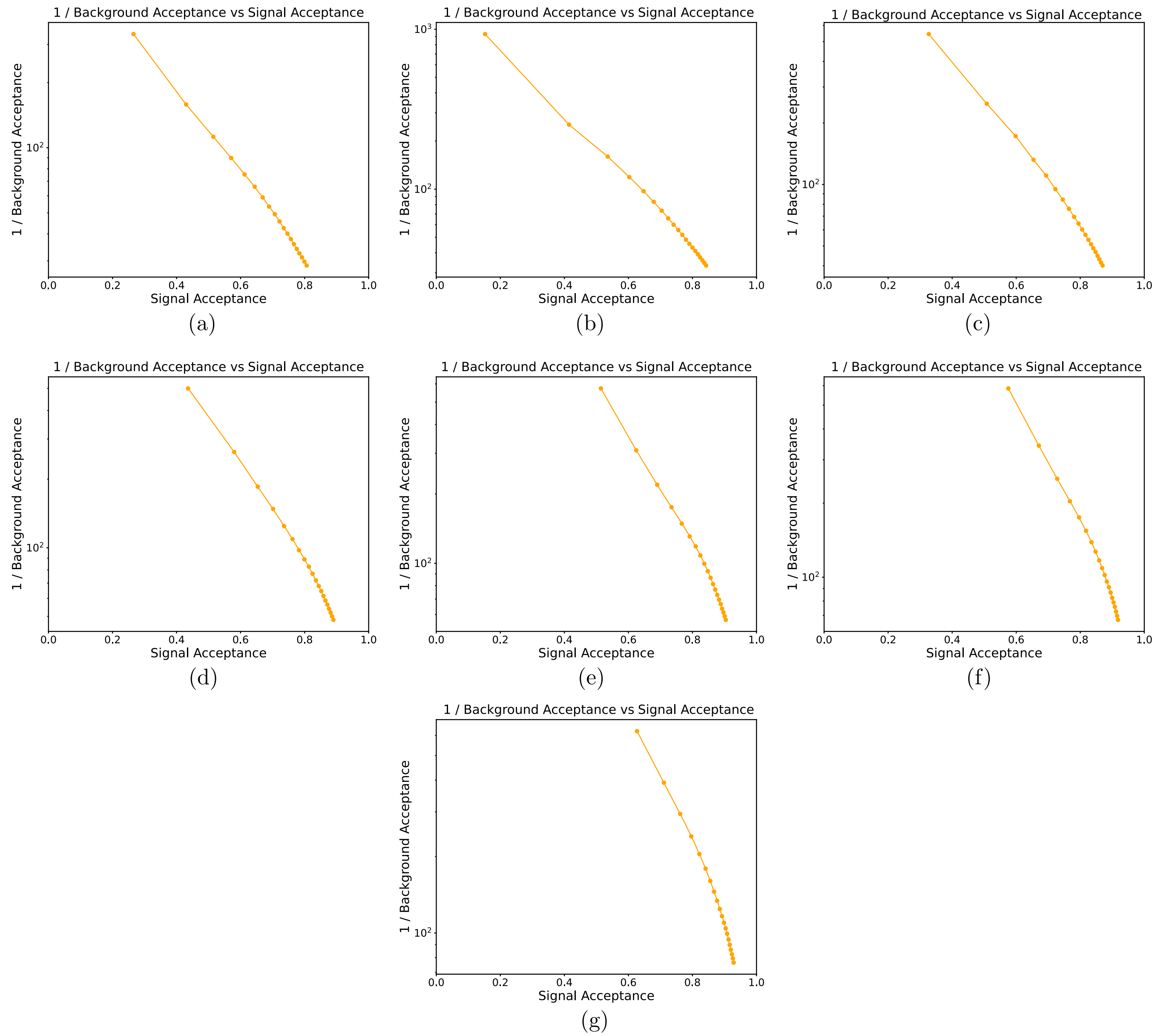

FIG. 10. 1/background acceptance against the signal acceptance for $h \to b\bar{b}$ channel. (a) $M_{H_F} = 800$ GeV, (b) $M_{H_F} = 900$ GeV, (c) $M_{H_F} = 1000$ GeV, (d) $M_{H_F} = 1100$ GeV, (e) $M_{H_F} = 1200$ GeV, (f) $M_{H_F} = 1300$ GeV and (g) $M_{H_F} = 1400$ GeV.

increases around 1.3 TeV; this can be explained by the slightly better performance of the BDT for the 1.3 TeV mass regarding 1.2 TeV.

Meanwhile, Fig. 12 shows the *signal significance* as a function of luminosity and the flavon mass M_{H_F} for the $pp \to H_F \to hb\bar{b}(h \to \gamma\gamma)$ process. In this channel, the sensitivity is lower than in the previous one because there is a factor of 10^{-3} that suppresses the previous case; such a factor comes from the $\mathcal{BR}(h \to \gamma\gamma) \sim 10^{-3}$. However, considering that a future 100 TeV collider is a possibility [40], it is important to note that our calculations estimate that for a luminosity of 30 ab^{-1}, the sensitivity could reach up to 5σ.

Finally, to highlight the usefulness of BDT, in Table VIII we present the *signal significance* for the $h \to b\bar{b}$ channel, where we have considered the basic cut, included in the HL-LHC card [41], and the following kinematic cuts for $M_{H_F} = 800$ GeV:

(1) $p_T(b_{1,2,3,4}) > 80, 60, 50, 25$ GeV,
(2) $650 < M_{\mathrm{inv}}(b_1 b_2 b_3 b_4) < 900$ GeV, and
(3) Combined transverse momentum $p_T(b_1 b_2 b_3 b_4) > 550$ GeV.

Therefore, we conclude that the use of BDT substantially improves the isolation of the proposed signals.

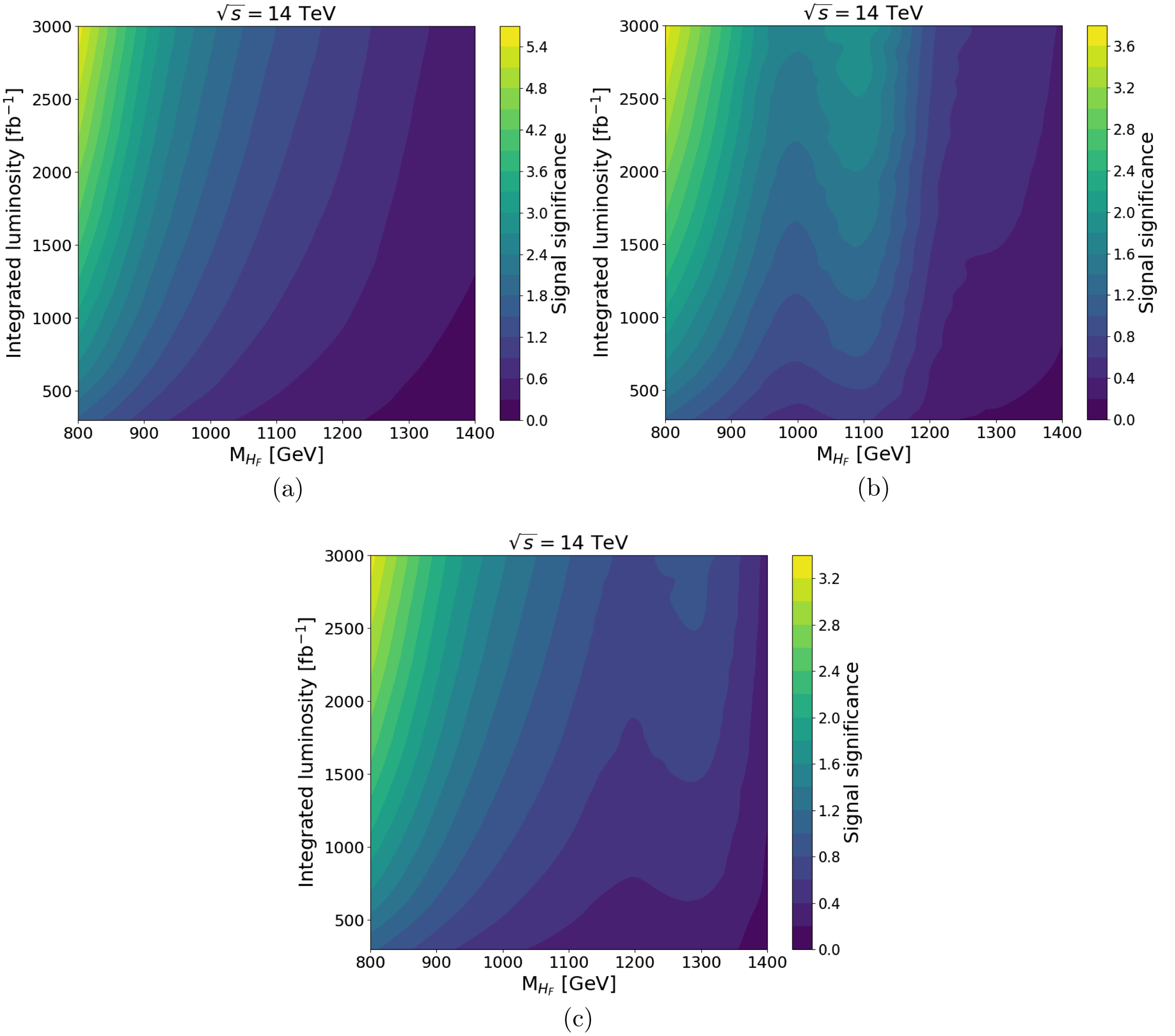

FIG. 11. Density plot showing the *signal significance* for the $h \to b\bar{b}$ channel as a function of the integrated luminosity and the flavon mass M_{H_F}: (a) **S1**, (b) **S2**, and (c) **S3**.

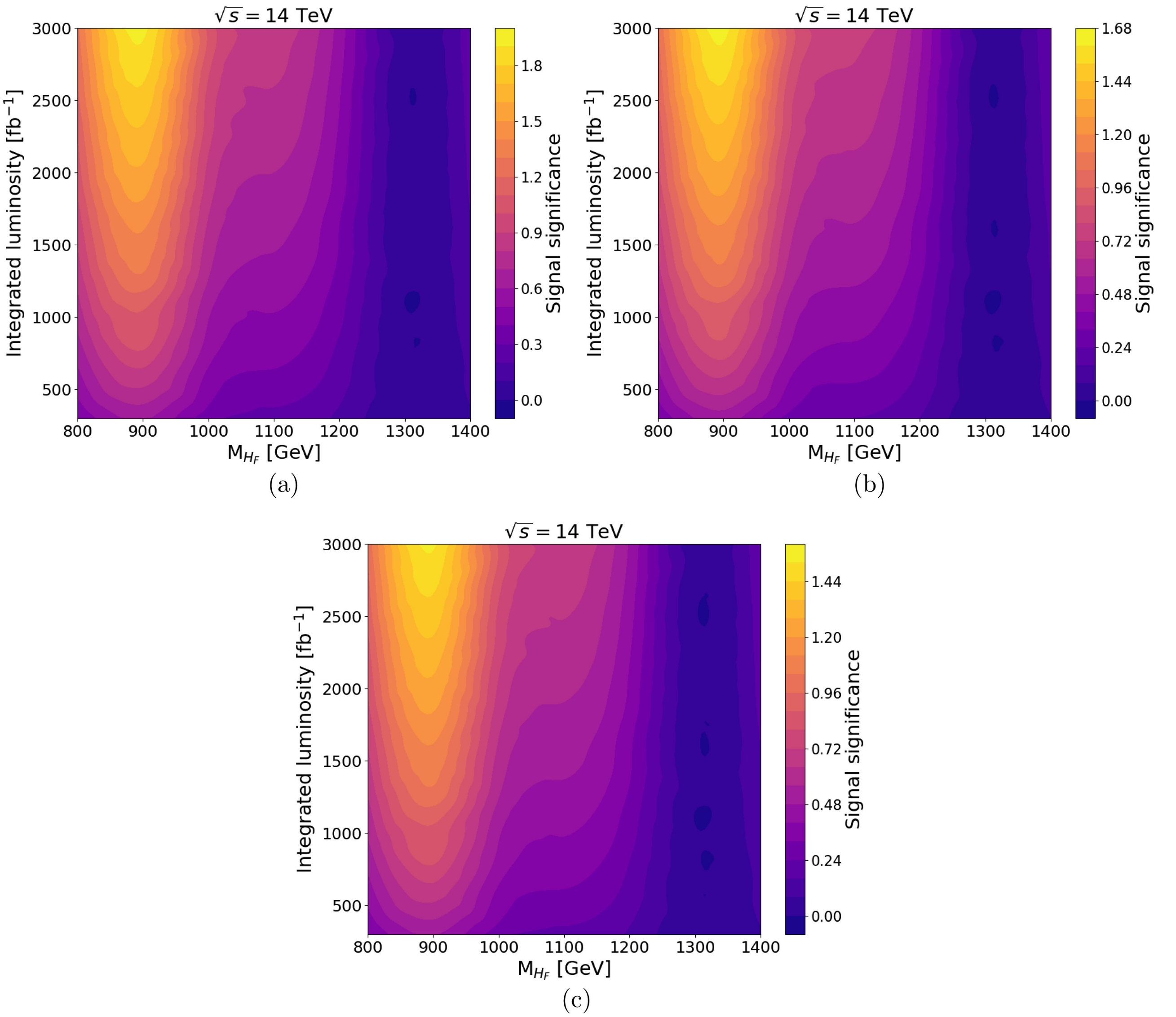

FIG. 12. Density plot showing the *signal significance* for the $h \to \gamma\gamma$ channel as a function of the integrated luminosity and the flavon mass M_{H_F}: (a) **S1**, (b) **S2**, and (c) **S3**.

TABLE VIII. Signal significance for the channel $h \to b\bar{b}$ and $\mathcal{L}_{\text{int}} = 3000$ fb^{-1}.

M_{H_F} (GeV)	Signal significance
800	1.75σ
900	0.87σ
1000	0.4872σ

V. CONCLUSIONS

In this paper we studied the possibility of observing the $pp \to H_F \to hb\bar{b}$ process through two channels in which the Higgs boson decays, namely, $h \to b\bar{b}$ and $h \to \gamma\gamma$. The H_F mother particle is a predicted state in a model that extends the Standard Model and incorporates the Froggatt-Nielsen mechanism which is an opportunity to explain the mass hierarchy. Our predictions consider realistic scenarios for the free parameters of the model, which were extracted by analyzing theoretical and experimental constraints. We identify specific regions of the model parameter space in which we found *signal significances* of up to 5σ (2σ) for the $h \to b\bar{b}$ ($h \to \gamma\gamma$) channel. The study was based on the High Luminosity Large Hadron Collider which aims 3000 fb^{-1} of accumulated data at 14 TeV.

ACKNOWLEDGMENTS

The work of Marco A. Arroyo-Ureña and T. Valencia-Pérez is supported by “Estancias posdoctorales por México (SECIHTI)” and “Sistema Nacional de Investigadores” (SNII-SECIHTI). T. V. P. acknowledges support from the

UNAM Project PAPIIT No. IN111224 and the SECIHTI Project No. CBF2023-2024-548 (formerly CONAHCYT). E. A. Herrera-Chacón acknowledges support from SECIHTI.

DATA AVAILABILITY

No data were created or analyzed in this study.

[1] G. Aad *et al.* (ATLAS Collaboration), Observation of a new particle in the search for the standard model Higgs boson with the ATLAS detector at the LHC, Phys. Lett. B **716**, 1 (2012).

[2] S. Chatrchyan *et al.* (CMS Collaboration), Observation of a new boson at a mass of 125 GeV with the CMS experiment at the LHC, Phys. Lett. B **716**, 30 (2012).

[3] G. Aad *et al.* (ATLAS Collaboration), Search for nonresonant pair production of Higgs bosons in the bb⁻bb⁻ final state in pp collisions at s = 13 TeV with the ATLAS detector, Phys. Rev. D **108**, 052003 (2023).

[4] G. Aad *et al.* (ATLAS Collaboration), Search for pair production of boosted Higgs bosons via vector-boson fusion in the $b\bar{b}b\bar{b}$ final state using pp collisions at $\sqrt{s} =$ 13 TeV with the ATLAS detector, Phys. Lett. B **858**, 139007 (2024).

[5] G. Aad *et al.* (ATLAS Collaboration), Studies of new Higgs boson interactions through nonresonant HH production in the $b\bar{b}\gamma\gamma$ final state in pp collisions at $\sqrt{s} =$ 13 TeV with the ATLAS detector, J. High Energy Phys. 01 (2024) 066.

[6] G. Aad *et al.* (ATLAS Collaboration), Search for the non-resonant production of Higgs boson pairs via gluon fusion and vector-boson fusion in the $b\bar{b}\tau^+\tau^-$ final state in proton-proton collisions at $\sqrt{s} = 13$ TeV with the ATLAS detector, Phys. Rev. D **110**, 032012 (2024).

[7] G. Aad *et al.* (ATLAS Collaboration), Search for non-resonant Higgs boson pair production in the $2b + 2\ell + E_T^{\mathrm{miss}}$ final state in pp collisions at $\sqrt{s} = 13$ TeV with the ATLAS detector, J. High Energy Phys. 02 (2024) 037.

[8] C. D. Froggatt and H. B. Nielsen, Hierarchy of quark masses, Cabibbo angles and CP violation, Nucl. Phys. **B147**, 277 (1979).

[9] M. Bauer, T. Schell, and T. Plehn, Hunting the flavon, Phys. Rev. D **94**, 056003 (2016).

[10] E. Barradas-Guevara, J. L. Diaz-Cruz, O. Félix-Beltrán, and U. J. Saldana-Salazar, Linking LFV Higgs decays $h \to \ell_i \ell_j$ with CP violation in multi-scalar models, arXiv:1706.00054.

[11] M. A. Arroyo-Ureña, A. Chakraborty, J. Lorenzo Díaz-Cruz, D. K. Ghosh, N. Khan, and S. Moretti, Flavon signatures at the HL-LHC, Phys. Rev. D **108**, 095026 (2023).

[12] M. A. Arroyo-Ureña, J. L. Díaz-Cruz, G. Tavares-Velasco, A. Bolaños, and G. Hernández-Tomé, Searching for lepton flavor violating flavon decays at hadron colliders, Phys. Rev. D **98**, 015008 (2018).

[13] M. A. Arroyo-Ureña, A. Fernández-Téllez, and G. Tavares-Velasco, Flavor changing flavon decay $\phi \to tc$ ($\phi = H_F, A_F$) at the high luminosity Large Hadron Collider, Rev. Mex. Fis. **69**, 020803 (2023).

[14] N. Khan and S. Rakshit, Study of electroweak vacuum metastability with a singlet scalar dark matter, Phys. Rev. D **90**, 113008 (2014).

[15] G. Cynolter, E. Lendvai, and G. Pocsik, Note on unitarity constraints in a model for a singlet scalar dark matter candidate, Acta Phys. Pol. B **36**, 827 (2005), arXiv:hep-ph/0410102.

[16] G. Aad *et al.* (ATLAS Collaboration), Search for Higgs boson pair production in the two bottom quarks plus two photons final state in pp collisions at $\sqrt{s} = 13$ TeV with the ATLAS detector, Phys. Rev. D **106**, 052001 (2022).

[17] S. Navas *et al.* (Particle Data Group), Review of particle physics, Phys. Rev. D **110**, 030001 (2024).

[18] A. M. Sirunyan *et al.* (CMS Collaboration), Search for lepton-flavor violating decays of the Higgs boson in the $\mu\tau$ and $e\tau$ final states in proton-proton collisions at $\sqrt{s} = 13$ TeV, Phys. Rev. D **104**, 032013 (2021).

[19] G. Aad *et al.* (ATLAS Collaboration), Searches for lepton-flavour-violating decays of the Higgs boson into $e\tau$ and $\mu\tau$ in $\sqrt{s} = 13$ TeV pp collisions with the ATLAS detector, J. High Energy Phys. 07 (2023) 166.

[20] M. A. Arroyo-Ureña, R. Gaitán, and T. A. Valencia-Pérez, SpaceMath version 1.0 a *Mathematica* package for beyond the standard model parameter space searches, Rev. Mex. Fis. E **19**, 020206 (2022).

[21] A. J. Buras, F. D. Fazio, J. Girrbach, R. Knegjens, and M. Nagai, The anatomy of neutral scalars with FCNCs in the flavour precision era, J. High Energy Phys. 06 (2013) 111.

[22] A. Crivellin, A. Kokulu, and C. Greub, Flavor-phenomenology of two-Higgs-doublet models with generic Yukawa structure, Phys. Rev. D **87**, 094031 (2013).

[23] M. Bona *et al.*, Model-independent constraints on $\delta f = 2$ operators and the scale of new physics, J. High Energy Phys. 03 (2008) 049.

[24] A. J. Bevan *et al.* (UTfit Collaboration), The UTfit Collaboration average of d meson mixing data: Winter 2014, J. High Energy Phys. 03 (2014) 123.

[25] G. Abbas, A. K. Alok, N. R. S. Chundawat, N. Khan, and N. Singh, Finding flavons at colliders, Phys. Rev. D **110**, 115015 (2024).

[26] T. Plehn, Lectures on LHC physics, Lect. Notes Phys. **844**, 1 (2012).

[27] A. Pak, M. Rogal, and M. Steinhauser, Production of scalar and pseudo-scalar Higgs bosons to next-to-next-to-leading order at hadron colliders, J. High Energy Phys. 09 (2011) 088.

[28] D. de Florian *et al.* (LHC Higgs Cross Section Working Group), Handbook of LHC Higgs cross sections: 4. Deciphering the nature of the Higgs sector, arXiv:1610.07922.

[29] A. Alloul, N. D. Christensen, C. Degrande, C. Duhr, and B. Fuks, FeynRules 2.0—A complete toolbox for tree-level

phenomenology, Comput. Phys. Commun. **185**, 2250 (2014).

[30] J. Alwall, R. Frederix, S. Frixione, V. Hirschi, F. Maltoni, O. Mattelaer, H. S. Shao, T. Stelzer, P. Torrielli, and M. Zaro, The automated computation of tree-level and next-to-leading order differential cross sections, and their matching to parton shower simulations, J. High Energy Phys. 07 (2014) 079.

[31] T. Sjöstrand, S. Ask, J. R. Christiansen, R. Corke, N. Desai, P. Ilten, S. Mrenna, S. Prestel, C. O. Rasmussen, and P. Z. Skands, An introduction to Pythia 8.2, Comput. Phys. Commun. **191**, 159 (2015).

[32] J. de Favereau, C. Delaere, P. Demin, A. Giammanco, V. Lemaître, A. Mertens, and M. Selvaggi (DELPHES 3 Collaboration), DELPHES 3, A modular framework for fast simulation of a generic collider experiment, J. High Energy Phys. 02 (2014) 057.

[33] M. Cacciari, G. P. Salam, and G. Soyez, FastJet user manual, Eur. Phys. J. C **72**, 1896 (2012).

[34] E. Conte, B. Fuks, and G. Serret, MadAnalysis 5, A user-friendly framework for collider phenomenology, Comput. Phys. Commun. **184**, 222 (2013).

[35] M. Cacciari, G. P. Salam, and G. Soyez, The anti-k_t jet clustering algorithm, J. High Energy Phys. 04 (2008) 063.

[36] G. Aad *et al.* (ATLAS Collaboration), Fast b-tagging at the high-level trigger of the ATLAS experiment in LHC Run 3, J. Instrum. **18**, P11006 (2023).

[37] L. Breiman *et al.*, *Classification and Regression Trees* (Wadsworth International Group, California, USA, 1984).

[38] T. Chen and C. Guestrin, XGBoost: A scalable tree boosting system, in *Proceedings of 22nd ACM SIGKDD International Conference on Knowledge Discovery and Data Mining, KDD '16* (ACM, New York, NY, USA, 2016), p. 785.

[39] J. Bergstra, D. Yamins, and D. Cox, Making a science of model search: Hyperparameter optimization in hundreds of dimensions for vision architectures, in *Proceedings of the 30th International Conference on Machine Learning*, edited by S. Dasgupta and D. McAllester, Vol. 28 of Proceedings of Machine Learning Research (PMLR, Atlanta, Georgia, USA, 2013), pp. 115–123, https://proceedings.mlr.press/v28/bergstra13.html.

[40] N. Arkani-Hamed, T. Han, M. Mangano, and L.-T. Wang, Physics opportunities of a 100 TeV proton–proton collider, Phys. Rep. **652**, 1 (2016).

[41] M. Selvaggi, Beta card for HL-LHC and HE-LHC studies, https://github.com/delphes/delphes/blob/master/cards/delphes_card_HLLHC.tcl (2017).